Microchimica Acta (2022) 189: 242
https://doi.org/10.1007/s00604-022-05344-z

ORIGINAL PAPER

Electrochemical α-fetoprotein immunosensor based on Fe_3O_4NPs@covalent organic framework decorated gold nanoparticles and magnetic nanoparticles including SiO_2@TiO_2

Ömer Saltuk Bölükbaşi[1] · Bahar Bankoğlu Yola[2] · Ceren Karaman[3] · Necip Atar[4] · Mehmet Lütfi Yola[5]

Received: 31 January 2022 / Accepted: 15 May 2022 / Published online: 2 June 2022

Abstract

The early diagnosis of major diseases such as cancer is typically a major issue for humanity. Human α-fetoprotein (AFP) as a sialylated glycoprotein is of approximately 68 kD molecular weight and is considered to be a key biomarker, and an increase in its level indicates the presence of liver, testicular, or gastric cancer. In this study, an electrochemical AFP immunosensor based on Fe_3O_4NPs@covalent organic framework decorated gold nanoparticles (Fe_3O_4 NPs@COF/AuNPs) for the electrode platform and double-coated magnetic nanoparticles (MNPs) based on SiO_2@TiO_2 (MNPs@SiO_2@TiO_2) nanocomposites for the signal amplification was fabricated. The immobilization of anti-AFP capture antibody was successfully performed on Fe_3O_4 NPs@COF/AuNPs modified electrode surface by amino-gold affinity, while the conjugation of anti-AFP secondary antibody on MNPs@SiO_2@TiO_2 was achieved by the electrostatic/ionic interactions. Transmission electron microscopy (TEM), X-ray diffraction (XRD), Fourier transform infrared spectroscopy (FTIR) analysis, cyclic voltammetry (CV), square wave voltammetry (SWV), and electrochemical impedance spectroscopy (EIS) techniques were used to characterize the nanostructures in terms of physical and electrochemical features. The limit of detection (LOD) was 3.30 fg mL^{-1}. The findings revealed that the proposed electrochemical AFP immunosensor can be effectively used to diagnose cancer.

Keywords α-Fetoprotein · Voltammetry · Nanocomposite · Immunosensor

Introduction

Cancer, which is one of the most serious risks to human health, is a disease that may be cured with a high rate or the adverse effects of it may be reduced if early detection and treatment approaches are developed [1]. Hence, from the past to the present, a great deal of study in the field of cancer has been focused on developing the appropriate and early diagnosis of the disease. α-Fetoprotein (AFP), an important tumor biomarker of primary lung cancer, gonadal or extragonadal yolk sac tumor, testicular tumor, or gastric cancer, is a glycoprotein with a molecular weight of ca.70 kDa and produced by the yolk sac and liver during the early embryonic period [2–4]. It has been reported that the concentration of AFP, which is approximately 25.0 ng mL^{-1} in healthy human blood serum, reached approximately 30-folds of it in cancer patients [5–9]. Therefore, engineering high sensitivity, selective, rapid, and efficient analytical methods for the quantitative determination of AFP level in human plasma is of great importance for cancer diagnosis. Until now, numerous analytical methods including enzyme-linked immunosorbent assay [10], electrochemiluminescence [11], surface plasmon resonance imaging [12], radioimmunoassay [13], fluorescence [14], and atomic absorption spectrometry [15] techniques have been suggested for the monitoring of AFP level. Although most of these methods have advantages such as broad detection range and low determination limit, they

✉ Mehmet Lütfi Yola
mlutfi.yola@hku.edu.tr

[1] Department of Metallurgical and Materials Engineering, Faculty of Engineering and Natural Sciences, Iskenderun Technical University, Iskenderun, Hatay, Turkey

[2] Department of Engineering Basic Sciences, Faculty of Engineering and Natural Sciences, Gaziantep Islam Science and Technology University, Gaziantep, Turkey

[3] Department of Electricity and Energy, Vocational School of Technical Sciences, Akdeniz University, Antalya, Turkey

[4] Department of Chemical Engineering, Faculty of Engineering, Pamukkale University, Denizli, Turkey

[5] Department of Nutrition and Dietetics, Faculty of Health Sciences, Hasan Kalyoncu University, Gaziantep, Turkey

are not effective due to the high cost, long time of analysis, and even their complicated processes [16–18]. Therefore, there is still a need for a cost-effective, swift, high accuracy, and easily applicable alternative method for the monitoring of AFP level.

Electrochemical immunosensors provide a number of advantages over other techniques, including a simple application procedure, instrument simplicity, small sample volumes, good sensitivity, and selectivity [19, 20]. It is also possible to boost the detection capability of the electrochemical sensors with some modifications. The signal amplification strategy is the most favored and adequate method for increasing their sensitivity [21]. Recently, numerous types of nanostructures such as carbonaceous materials, quantum dots, metal oxides, metal sulfides, and metal nanoparticles have been employed to amplify the performance of the electrochemical immunosensor. In literature, some AFP electrochemical immunosensors were presented for highly selective assay. For example, Eu-MOF nanorods functionalized with heterocyclic ionic liquid were prepared and utilized for photoelectrochemical immunoassay of AFP. The photoelectrochemical immunosensor showed a LOD of 0.16 pg mL^{-1} [22]. In addition, CoFe Prussian blue analog combined PdAg hybrid nanodendrites were produced for electrochemical sensing of AFP. The fabricated immunosensor demonstrated a linear range of 100.00 fg mL^{-1}–200.00 ng mL^{-1} and a LOD of 18.60 fg mL^{-1} at the optimal operating conditions [23]. Finally, photoelectrochemical AFP immunosensor based on MIL-101(Cr) and CdSe quantum dots was developed. The AFP immunosensor can not only provide highly sensitive detection, but also provide the high accuracy and assay ability. Thus, the prepared photoelectrochemical AFP immunosensor showed a LOD of 0.054 ng mL^{-1} [3]. Hence, the applicability of electrochemical immunosensor technology for the high sensitivity and selectivity determination of AFP appears to be appropriate.

Metal nanoparticles as a significant catalyst in biosensor applications have been frequently used owing to a simple synthesis process with minimal waste, efficient surface modification, and high stability [24, 25]. They have been usually incorporated into two- (2D) or three-dimensional (3D) nanomaterials via chemical reduction reaction since they can prevent aggregation, thanks to their high surface energies [26, 27]. Nonetheless, their irregular distributions on 2D or 3D nanostructures may directly affect the efficient contact area in between the substrate and target molecules, resulting in a decrease in the catalytic performance of the hybrid nanomaterial. Hence, bearing the aforementioned obstacles in mind, in this work, it was aimed to fabricate the three-dimensional Fe_3O_4NPs@covalent organic framework (COF) decorated gold nanoparticles to get benefit from its superior catalytic features. Porous framework materials as COFs have great interest for biosensor applications. COFs serve as electrochemical transducers for modification material to improve the surface areas, crystallinity, and thermal stability [28–30]. Hence, the uniform incorporation of COFs into Fe_3O_4NPs@COF/AuNPs architecture not only avoid AuNPs' accumulation but also enhance nanoparticles' order, providing the contact between the substrate and target molecules. Hence, it is expected that the proposed immunosensor system will offer a promising electrochemical performance.

Magnetic nanoparticles (MNPs) have been recently investigated in nanotechnology applications such as nanosensor/biosensor development, environmental water treatment, and industrial effluents [31, 32]. Especially, iron oxide–based MNPs such as magnetite (Fe_3O_4) and maghemite (γ-Fe_2O_3) demonstrate noteworthy magnetic properties [33]. Thus, the employment of these nanostructures in environmental or medical applications could be an important tool owing to easy separation via magnetic field, providing environmentally friendly production. Several techniques including the sol–gel approach, microemulsion, and hydro- or solvothermal production pathways can be utilized for the fabrication of MNPs [34]. The reactions in hydrothermal method can take place in an aqueous solution in a reactor/autoclave at about 200 °C [35], as such high temperatures provide efficient nucleation and nanoparticles having the increased growth, resulting in MNPs' formation [34]. Nonetheless, due to the tendency of aggregation of the nanoparticles, the stabilization of MNPs is a critical problem. MNP functionalization by organic/inorganic agents is an efficient technique to overcome this challenge [32]. For example, MNP coating is commonly utilized for the development of core–shell structures especially in environmental remediation applications.

Mesoporous silica is one of the most important coating materials and offers a high surface area with ordered pore size, thereby preventing aggregation [31]. Especially, sol–gel method is frequently utilized for mesoporous silica preparation. According to the Stöber method, the alkyl silicates' hydrolysis can occur in alcoholic solutions and silicic acid's condensation is performed by NH_3 catalyst [36].

TiO_2, on the other hand, has recently garnered substantial attention owing to heterogeneous nature and the reusability properties. In addition, it can be employed in long-term applications [37]. Although TiO_2 and its composites can be utilized as catalysts thanks to their high solubility in water, because of the high-cost process in phase separation, there are some disadvantages for large-scale utility. These nanocomposites can be engineered by some specific methods such as solvothermal, pyrolysis, and sonochemistry [38]. Especially, the growth of the produced nanoparticles can be controlled the by sol–gel technique [39].

Herein, an electrochemical α-fetoprotein immunosensor based on Fe_3O_4 NPs@COF/AuNPs as the electrode platform and double-coated magnetic nanoparticles based on the signal amplification was proposed for the first time. The

exceptional selectivity with no interference in real samples enhanced sensitivity with the limit of detection value of 3.30 fg mL^{-1} and convenience of usage, as well as environment and health compliance were all acquired by the fabricated electrochemical AFP immunosensor. As a result, this research lays the framework for the development of a highly selective and sensitive electrochemical AFP immunosensor for cancer diagnostics.

Experimental section

Materials

α-Fetoprotein (AFP), anti-AFP capture antibody (anti-AFP-Ab_1), anti-AFP secondary antibody (anti-AFP-Ab_2), prostate-specific antigen (PSA), carcinoembryonic antigen (CEA), bovine serum albumin (BSA), squamous cell carcinoma antigen (SCCA), human serum albumin (HSA), neuron-specific enolase (NSE), human immunoglobulin (IgG), L-cysteine (L-CYS), glucose (GLU), iron(III) chloride hexahydrate ($FeCl_3{\cdot}6H_2O$), iron(II) chloride tetrahydrate ($FeCl_2{\cdot}4H_2O$), ammonium hydroxide (NH_4OH), 1,3,5-tris (4-aminophenyl) benzene (TAPB), 2,5-dimethoxyterephtaldeyde (DMTP), chloroauric acid ($HAuCl_4{\cdot}3H_2O$), sodium borohydride ($NaBH_4$), ethylene glycol (EG), polyethylene glycol (PEG), tetraethyl orthosilicate (TEOS), and titanium(IV) isopropoxide (TIP) were acquired from Sigma-Aldrich. The phosphate-buffered saline (PBS) with a concentration of 0.1 mol L^{-1} and the pH value of 7.0 was used as both a supporting electrolyte and dilution buffer solution.

Physicochemical and electrochemical characterization techniques

The surface morphologies of nanostructures were explored through JEOL 2100 TEM, whereas a Rigaku X-ray diffractometer ($\lambda = 0.154$ nm) was employed to collect XRD spectra to gain further knowledge about the crystalline structure of the nanomaterials. The electrochemical features of the developed electrochemical sensors, on the other hand, were evaluated by CV, EIS, and SWV techniques through Gamry Reference 600 workstation (Gamry, USA).

Fabrication of Fe_3O_4NP, Fe_3O_4NPs@COF, and Fe_3O_4NPs@COF/AuNP nanocomposites

Following the preparation of $FeCl_3{\cdot}6H_2O$ (2.0 g) and $FeCl_2{\cdot}4H_2O$ (1.0 g) solution in de-ionized (DI) water (25.0 mL), NH_4OH (30.0%, 5.0 mL) was gently introduced into the preceding solution at 25 °C under stirring over 30 min, and pH was set to ca.10. The resultant Fe_3O_4NP was collected by a magnet and washed with ultra-pure water three times to eliminate the excess ammonia, followed by ***Fe_3O_4NP*** drying and storing at 25 °C [40].

After DMTP (100.0 mg) and TAPB (120.0 mg) were dissolved in mixture including butanol (25.0 mL) and 1,4-dioxane (25.0 mL), Fe_3O_4NPs (25.0 mg) was progressively added into the prepared DMTP-TAPB solution. After the addition of CH_3COOH (0.10 mL) was performed to the above solution under vigorous stirring at 25 °C over 90 min, ***Fe_3O_4NPs@COF*** was rinsed with DI water 3 times and allowed to dry at 25 °C.

The prepared Fe_3O_4NPs@COF (150.0 mg) was dissolved in tetrahydrofuran (40.0 mL), and $HAuCl_4{\cdot}3H_2O$ (0.1%, 10.0 mL in methanol) was added into Fe_3O_4NPs@COF solution and stirred vigorously at 25 °C for 90 min. ***Fe_3O_4NPs@COF/AuNP*** nanocomposite was collected using a magnet upon adding $NaBH_4$ (1.0 mol L^{-1}, 15.0 mL) solution to the aforesaid dispersion. It was then washed twice with DI water and allowed to be dried at ambient temperature [41].

Fabrication of electrochemical sensor platforms

The glassy carbon electrode (GCE) was kept ready for its upcoming use according to the previously described cleaning technique [42]. Over a 10-min period, alumina slurries of varied particle sizes (0.1 μm and 0.05 μm) were loaded onto cleaning pads, and GCE was gleamed with these alumina slurries. Fe_3O_4NPs@COF/AuNP dispersion (20.0 mL, 0.2 mg mL^{-1}) was deposited onto the surface of clean glassy carbon electrode after rinsed by acetonitrile at 25 °C to eradicate the remaining Al_2O_3. The infrared lamp was employed to evaporate the residual solvent over 30 min, resulting in Fe_3O_4NPs@COF/AuNPs modified GCEs (***Fe_3O_4NPs@COF/AuNPs/GCE***). Eventually, the same technique was implemented to construct Fe_3O_4NPs@COF modified GCE (***Fe_3O_4NPs@COF/GCE)***.

A total of 20.0 μL of anti-AFP-Ab_1 solution (20.0 μg mL^{-1}) was poured over Fe_3O_4NPs@COF/AuNPs/GCE, leading to ***anti-AFP-Ab_1/Fe_3O_4NPs@COF/AuNPs/GCE*** through amino-gold affinity among the primer anti-AFP-Ab_1 and Fe_3O_4NPs@COF/AuNPs/GCE over 20 min at a temperature of 37.0 °C. Subsequently, BSA (2.0% w/v) was dropped on anti-AFP-Ab_1/Fe_3O_4NPs@COF/AuNPs/GCE at the same operating conditions and duration to abolish the non-specific interactions (***BSA/anti-AFP-Ab_1/Fe_3O_4NPs@COF/AuNPs/GCE***). Following the incubation of antigen AFP proteins with varied concentrations on BSA/anti-AFP-Ab_1/Fe_3O_4NPs@COF/AuNPs/GCE via antibody-antigen interaction, the eventual electrode (***AFP/BSA/anti-AFP-Ab_1/Fe_3O_4NPs@COF/AuNPs/GCE***) was washed by PBS solution to detach non-contacted proteins.

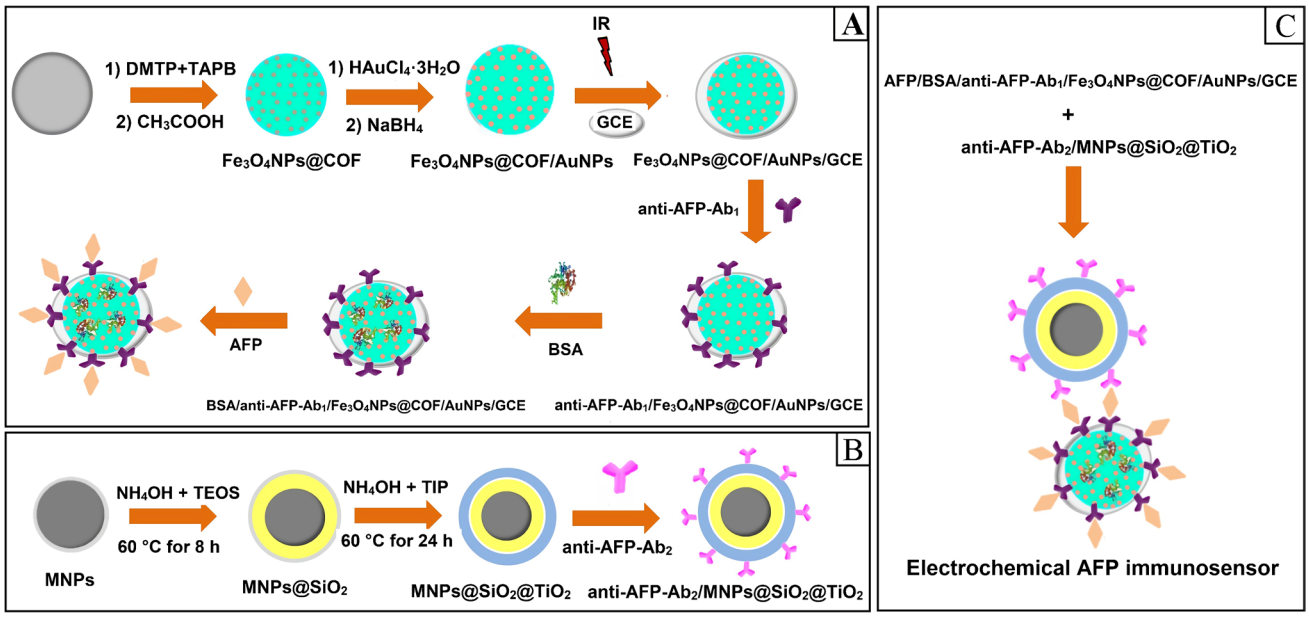

Scheme 1 Schematic illustration of the fabrication procedure of electrochemical AFP immunosensor

Fabrication of MNP, MNPs@SiO_2, and MNPs@SiO_2@TiO_2 nanostructures and signal amplification and anti-AFP-Ab_2 conjugation procedures

Upon the fabrication of $FeCl_3{\cdot}6H_2O$ (20.0 mmol) solution in EG (100.0 mL) at 80 °C under vigorous stirring, PEG (4.0 g) and sodium acetate (100.0 mmol) solution were introduced to this solution. The *MNP* was acquired by thermal treatment of the resultant dispersion at 200 °C over 8 h. The resultant powder was washed with ethanol twice times and stored at 25 °C [43].

After dispersing MNPs (4.0 mg) in sodium acetate (1.0 mol, 100.0 mL) at 80 °C for 8 h via ultrasonication, NH_4OH (30.0%, 5.0 mL), TEOS (2.0 mL), and ethanol (5.0 mL) were introduced into the MNP dispersion under strong stirring at 60 °C for 8 h. Finally, the obtained ***MNPs@SiO₂*** was washed with ethanol twice times and stored at 25 °C [44].

For MNPs@SiO_2@TiO_2 preparation, following the stabilization of MNPs@SiO_2 by sodium acetate, it was dispersed in ethanol (100.0 mL) by ultrasonication. Subsequently, NH_4OH (30.0%, 5.0 mL) and TIP (2.0 mL) were added into the resultant stabilized MNPs@SiO_2 dispersion under strong stirring at 60 °C for 24 h. The resulting ***MNPs@SiO₂@TiO₂*** was magnetically separated by an external magnet and preserved at 25 °C.

Following the getting ready of 20.0 µL anti-AFP-Ab_2 (20.0 µg mL^{-1}), anti-AFP-Ab_2 was interacted with MNPs@SiO_2@TiO_2 through sustained electrostatic/ionic attractions over 20 min at the operating temperature of 37.0 °C. Afterwards, the obtained ***anti-AFP-Ab₂/MNPs@SiO₂@TiO₂*** was preserved in a PBS solution.

The electrochemical performance evaluation of the constructed immunosensors

The eventual electrochemical AFP immunosensor was constructed as a result of the interactions among the AFP/BSA/anti-AFP-Ab_1/Fe_3O_4NPs@COF/AuNPs/GCE and anti-AFP-Ab_2/MNPs@SiO_2@TiO_2 through distinctive antibody-antigen dealings. A total of 25.0 µL of anti-AFP-Ab_2/MNPs@SiO_2@TiO_2 (20.0 mg mL^{-1}) was manufactured on AFP/BSA/anti-AFP-Ab_1/Fe_3O_4NPs@COF/AuNPs/GCE for 25 min to assure this interlinkage. The resultant AFP immunosensor (***TiO_2@SiO_2@MNPs@anti-AFP-Ab_2/AFP/BSA/anti-AFP-Ab_1/Fe_3O_4NPs@COF/AuNPs/GCE***) was held in PBS (3.0 mL, 0.1 mol L^{-1}, pH = 7). In all electrochemical tests, a normal three-electrode configuration electrochemical cell with Ag/AgCl (sat KCl) as a reference electrode and Pt-wire as a counter electrode was utilized. Even before conducting the electrochemical measurements, the solution including 1.0 mmol L^{-1} H_2O_2 in PBS solution was purged with argon gas (> 99.9%) over 5 min to eliminate the oxygen from the solution. A total of 1.0 mmol L^{-1} H_2O_2 was utilized as a redox probe thanks to its facile oxidation into oxygen, the stable electrostatic/ionic interactions on immunosensor surface, and preferable availability in immunosensor technology [45, 46]. After the purging treatment with argon gas (> 99.9%), the electrochemical potential in range from + 0.0 to + 0.3 V was applied to electrochemical cell

and the observed voltammograms were evaluated. Scheme 1 portrays a schematic illustration of the electrochemical AFP immunosensor fabrication pathway depending on the reaction of $H_2O_2 \leftrightarrow O_2 + 2H^+ + 2e^-$.

Pathway for sample preparation

The general technique to getting ready of the samples is discussed in detail in the Supplementary Data file [47].

Results and discussion

Characterizations of Fe_3O_4NPs@COF/AuNP nanocomposite

The structural characterization of Fe_3O_4NPs@COF/AuNP nanocomposite was carried out through TEM and HRTEM images (Fig. 1). According to Fig. 1A, Fe_3O_4NPs@COF/AuNP nanocomposite as core–shell nanospheres offered an average particle diameter of 600–700 nm. The outer shell with 120 nm and the uniform AuNPs with about 3–5 nm size confirmed the homogeneous distribution in the pore channels. In addition, AuNPs with 0.233-nm interplanar space and (111) plane in face centered cubic are observed in Fig. 1B. Hence, it was confirmed that the successful preparation of Fe_3O_4NPs@COF/AuNP nanocomposite was achieved in this study.

FTIR spectra (Fig. S1A) depicted the absorption peak at ca. 580 cm^{-1} that could be ascribed to Fe–O vibration, whereas the peaks at about 1600 and 1413 cm^{-1} were attributed to the asymmetric stretching and symmetric stretching, respectively, owing to –COOH groups on Fe_3O_4NPs structure. In the FTIR spectrum of Fe_3O_4NPs@COF, the absorption band belonging to –C = N– group was observed at about 1589 cm^{-1}. Following the inclusion of AuNPs into the pore space, the same absorption band detected at almost 1589 cm^{-1} proved the existence of the C = N– functionalities. Hence, it was revealed that the chemical structure of COFs could not be altered [48]. XRD spectra (Fig. S1B) depicted the crystal structures of Fe_3O_4NPs@COF and Fe_3O_4NPs@COF/AuNP nanocomposite. XRD peaks of Fe_3O_4NPs@COF at 29.91, 35.47, 42.97, 54.18, 57.49, and 63.13° were attributed to Fe_3O_4 phase. XRD peaks at 5.62, 7.50, 9.73, and 25.71° also corresponded to (200), (210), (220), and (001) planes of TAPB-and DMTP-based COF material, respectively [49]. Finally, the XRD pattern of Fe_3O_4NPs@COF/AuNP nanocomposite was almost the same in comparison with Fe_3O_4NPs@COF, suggesting the incorporation of AuNPs into Fe_3O_4@COF could not cause an important change in crystallinity owing to AuNPs' small dimension.

Characterizations of MNPs@SiO_2@TiO_2

TEM and HRTEM images were also acquired to assess the surface morphology of MNPs, MNPs@SiO_2, and MNPs@SiO_2@TiO_2 nanostructures (Fig. 2). The aggregated MNP is detected in Fig. 2A as a nanoflower-like morphology [50]. According to the HRTEM image of the smallest MNPs (Fig. 2B), it was confirmed that the synthesis of the smallest MNPs with about 4–6 nm size and 0.250-nm interplanar space attributing to (311) crystalline plane was successfully accomplished. In addition, it was concluded that these nanoparticles were aggregated as quasi-spherical with average size of 110 ± 2 nm (Fig. S2A). TEM image of MNPs@SiO_2 (Fig. 2C) confirmed the silica-coated magnetite nanoparticles having a core–shell structure. In addition, the average size of MNPs@SiO_2 was obtained as 150 ± 3 nm (Fig. S2B), and a silica layer thickness of about 18–20 nm was observed [51, 52]. TEM image of MNPs@SiO_2@TiO_2 (Fig. 2D) demonstrated the prepared double-layer coated MNPs with SiO_2 and TiO_2 by hydrolysis and condensation techniques, providing the growth of TiO_2 on silica layer, and its average

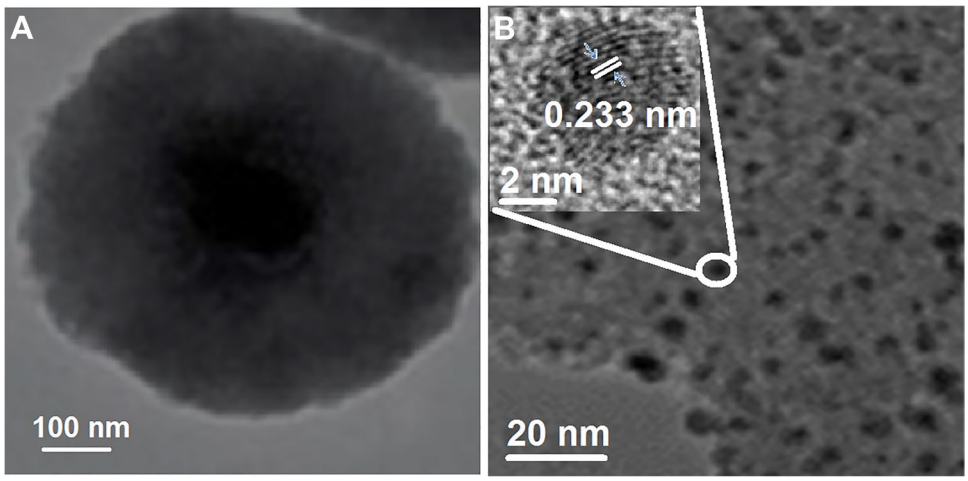

Fig. 1 **A** TEM and **B** HRTEM images of Fe_3O_4NPs@COF/AuNP nanocomposite

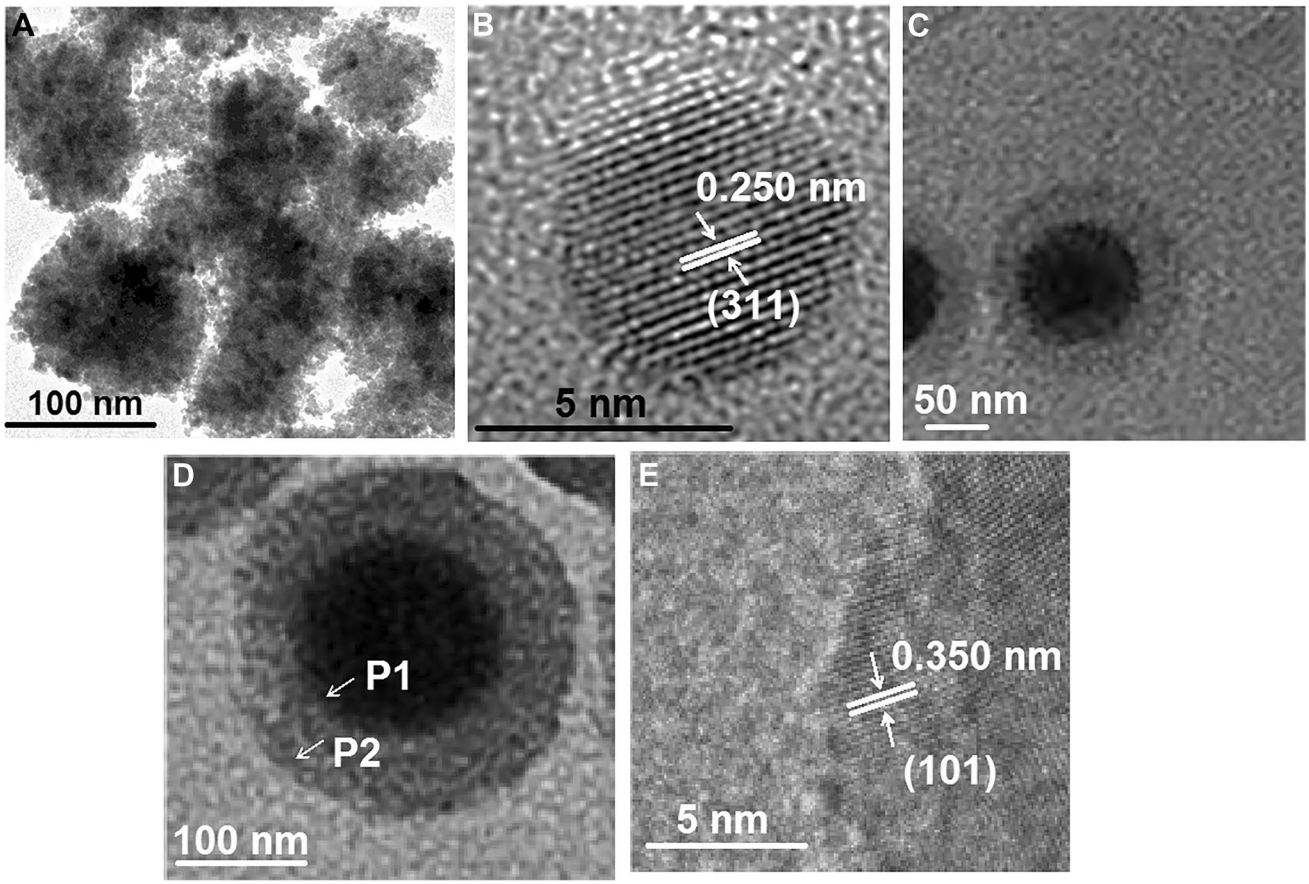

Fig. 2 **A** TEM image of MNPs, **B** HRTEM image of MNPs, **C** TEM image of MNPs@SiO_2, **D** TEM image of MNPs@SiO_2@TiO_2, and **E** HRTEM image of MNPs@SiO_2@TiO_2

size was calculated as 200 ± 2 nm (Fig. S2C). Furthermore, 0.350-nm interplanar space corresponding to (101) crystalline plane of TiO_2 phase was determined by HRTEM micrograph (Fig. 2E). EDX measurements (Fig. S3) were also conducted for the determination of chemical composition. In the P1 region of Fig. 2D, iron oxide presence was observed on the core region whereas titania and silica presence were observed majorly on the shell region (P2) of Fig. 2D, confirming the double coating of magnetite nanoparticles.

Magnetic features and their changes with the coating process were also explored. Figure 3 demonstrates the magnetization versus magnetic field plots of MNPs, MNPs@SiO_2, and MNPs@SiO_2@TiO_2 at 300 K (Fig. 3A) and 2 K (Fig. 3B). According to the inset of Fig. 3A, the coercive field and remanent magnetization were nearly zero at 300 K for MNPs, MNPs@SiO_2, and MNPs@SiO_2@TiO_2, revealing the superparamagnetism's thermal relaxation states after the coating. Nonetheless, the inset of Fig. 3B illustrates the hysteresis curves with non-zero coercive fields (Hc = about 195 Oe) for MNPs that remained unchanged during SiO_2 and SiO_2@TiO_2 coating. The values of the saturation magnetization for MNPs at 2 K and 300 K were computed as 85.2 emu g^{-1} and 75.1 emu g^{-1}, respectively. The saturation magnetization value at 2 K showed about 90% of the reported value for bulk magnetite (920–100 emu g^{-1}) [53]. The decrease on saturation magnetization value was corresponding to the magnetic surface disorder contributions, the oxidation of Fe^{2+}, and magnetite's crystallization during the synthesis. The saturation magnetization values of MNPs@SiO_2 and MNPs@SiO_2@TiO_2 were lower than that of MNPs, indicating the non-magnetic mass relating to MNPs@SiO_2@TiO_2 [54]. On the other hand, the values of the saturation magnetization for MNPs@SiO_2 and MNPs@SiO_2@TiO_2 at 2 K were determined as 17.6 and 10.3 emu g^{-1}, respectively. Due to the significant decrease of the saturation magnetization for MNPs@SiO_2@TiO_2, it could be separated by an external field.

The evaluation of the sensor platform and the signal amplification electrochemical performances

To evaluate the electrochemical performance of the constructed sensor platform in the existence of 1.0 mM $[Fe(CN)_6]^{3-/4-}$, CV and EIS were implemented. At first, by

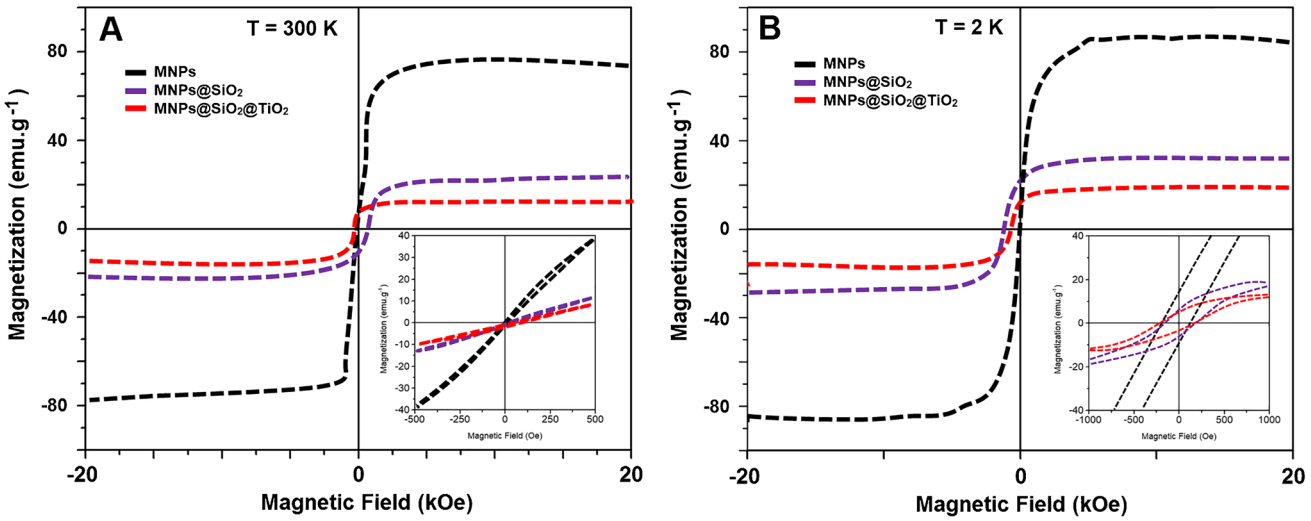

Fig. 3 Magnetization as a function of magnetic field curves **A** at 300 K and **B** at 2 K: Insets show the central regions of the hysteresis curves

using bare GCE, at the potentials of + 0.300 V and + 0.150 V, an anodic and a cathodic peak, respectively, were observed (curve (a) of Fig. 4A). Following the employment of Fe_3O_4NPs@COF/GCE (curve (b) of Fig. 4A), the substantial increment in the signals was detected due to the combined effect of Fe_3O_4NPs and COF providing the large surface area [48]. When Fe_3O_4NPs@COF/AuNPs/GCE (curve (c) of Fig. 4A) was applied to 1.0 mM $[Fe(CN)_6]^{3-/4-}$, the augmented electrochemical performance was achieved owing to AuNPs' superb conductivity and catalytic effect [55]. As predicted, the inhibiting effect of anti-AFP-Ab1 resulted in apparent decreases in anodic and cathodic signals (curve (d) of Fig. 4A). Furthermore, immobilizations of BSA (curve (e) of Fig. 4A) and antigen AFP (curve (f) of Fig. 4A) resulted in a significant electron transport preventing impact. Consequently, the immobilizations of BSA and antigen AFP were successful, as shown by curves (e) and (f) in Fig. 4A. Finally, additional declines in anodic and cathodic signals were recorded via the eventual immunosensor (curve (g) of Fig. 4A).

Following that, EIS measurements were used to validate the CV results (Fig. 4B). The charge transfer resistances were computed as 300 Ω for bare GCE (curve (a)), 260 Ω for Fe_3O_4NPs@COF/GCE (curve (b)), 180 Ω for Fe_3O_4NPs@COF/AuNPs/GCE (curve (c)), 200 Ω for anti-AFP-Ab_1/Fe_3O_4NPs@COF/AuNPs/GCE (curve (d)), 220 Ω for BSA/

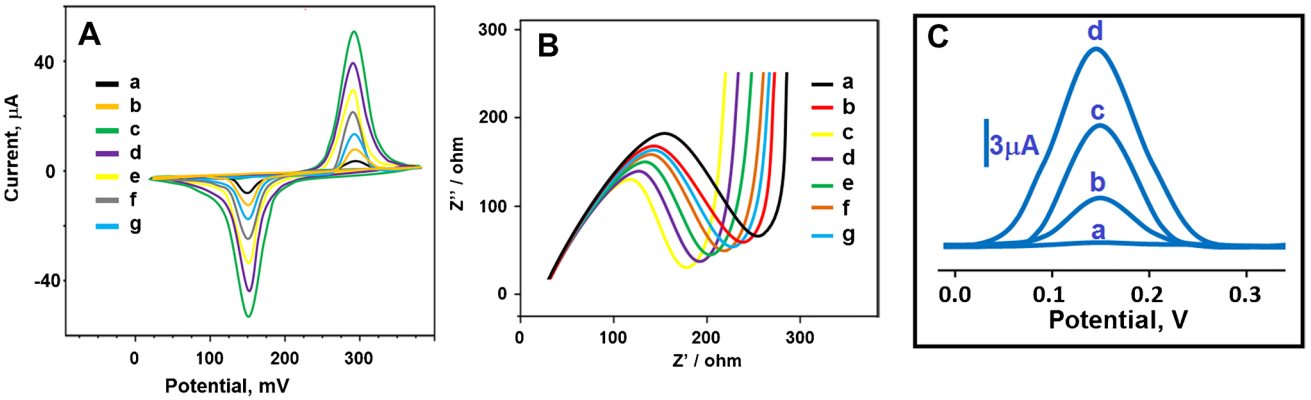

Fig. 4 **A** Cyclic voltammograms, **B** EIS responses at (a) bare GCE, (b) Fe_3O_4NPs@COF/GCE, (c) Fe_3O_4NPs@COF/AuNPs/GCE, (d) anti-AFP-Ab_1/Fe_3O_4NPs@COF/AuNPs/GCE, (e) BSA/anti-AFP-Ab_1/Fe_3O_4NPs@COF/AuNPs/GCE, (f) AFP/BSA/anti-AFP-Ab_1/Fe_3O_4NPs@COF/AuNPs/GCE, and (g) the final immunosensor including anti-AFP-Ab_1, antigen AFP, and anti-AFP-Ab_2 (scan rate of 100 mV s^{-1}) in 1.0 mmol L^{-1} $[Fe(CN)_6]^{3-}$ containing 0.1 mol L^{-1} KCl, and **C** SWV responses of the developed immunosensors incubated with 0.50 pg mL^{-1} antigen AFP using anti-AFP-Ab_2/MNPs (curve (b)), anti-AFP-Ab_2/MNPs@SiO_2 (curve (c)), and anti-AFP-Ab_2/MNPs@SiO_2@TiO_2 (curve (d)) in the absence of H_2O_2 (curve (a)) and in the presence of 1.0 mmol $L.^{-1}$ H_2O_2 (parameters are frequency of 100 Hz, pulse amplitude of 25 mV, scan increment of 5 mV for SWV measurements)

anti-AFP-Ab_1/Fe_3O_4NPs@COF/AuNPs/GCE (curve (e)), 240 Ω for AFP/BSA/anti-AFP-Ab_1/Fe_3O_4NPs@COF/AuNPs/GCE (curve (f)), and 250 Ω for the final immunosensor (curve (g)). As a result, the findings may point to the notion that CV and EIS results agreed well.

Finally, three separate electrochemical AFP immunosensors which comprised of 0.50 pg mL^{-1} antigen AFP were created employing various signal amplifications for the sequential electrochemical assessment of the obtained signal amplification (Fig. 4C). In this regard, anti-AFP-Ab_2/MNPs (curve (b)), anti-AFP-Ab_2/MNPs@SiO_2 (curve (c)), and anti-AFP-Ab_2/MNPs@SiO_2@TiO_2 (curve (d)) were used for 25 min. In the presence of 1.0 mM H2O2, SWV responses were obtained. The significant electrochemical signals (about 3.0 µA) at 0.15 V were monitored by using anti-AFP-Ab_2/MNPs (curve (b)). Due to MNPs@SiO_2's large surface area and electrochemical activity [56], the boosted electrochemical signals (about 7.5 µA) were acquired by using anti-AFP-Ab_2/MNPs@SiO_2 (curve (c)). Finally, the highest electrochemical immunosensor signals were recorded via anti-AFP-Ab_2/MNPs@SiO_2@TiO_2 (curve (d)) owing to superior biocompatibility, and the readily tailored surfaces [57, 58]. Finally, to confirm the enhancement of electrochemical activity resulted from surface area, the electrochemical surface areas of bare GCE, MNPs/GCE, MNPs@SiO_2/GCE, and MNPs@SiO_2@TiO_2/GCE were evaluated by the Randles–Sevcik formula ($i_p = 2.69 \times 10^5\ A\ n^{3/2}\ D^{1/2}\ C\ v^{1/2}$) [47, 59]. In conclusion, 0.174 ± 0.001 cm^2 for bare GCE, 0.541 ± 0.002 cm^2 for MNPs/GCE, 1.289 ± 0.001 cm^2 for MNPs@SiO_2/GCE, and 1.617 ± 0.003 cm^2 for MNPs@SiO_2@TiO_2/GCE were calculated, suggesting the obvious electrochemical surface enhancement.

Determining the optimal conditions

In optimization experiments, the effects of solution pH, immunological reaction time, H_2O_2, and anti-AFP-Ab_2/MNPs@SiO_2@TiO_2 solution concentration were explored in depth (Fig. S4).

Limit of detection and limit of quantification calculations

Figure 5 depicts the calibration equation (I (µA) = 22.407C_{AFP} (pg mL^{-1}) + 0.217, R^2 = 0.9978) obtained by escalating antigen AFP concentrations and SWV signals. The limit of quantification (LOQ) (Eq. 1) and limit of detection (Eq. 2) values were obtained as 0.01 pg mL^{-1} and 3.30 fg mL^{-1}, respectively.

$$\text{Limit of quantification} = 10.0S/m \quad (1)$$

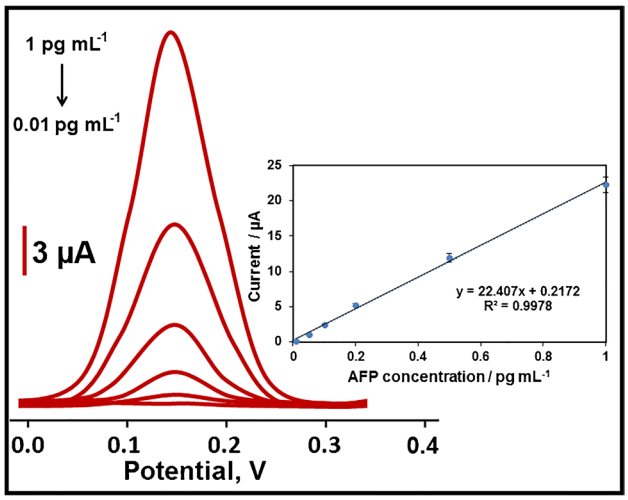

Fig. 5 Concentration effect (from 0.01 to 1.0 pg $mL.^{-1}$ AFP) on immunosensor signals. Inset: Calibration curve for electrochemical AFP immunosensor (potential range is + 0.0/ + 0.3 V; parameters are frequency of 100 Hz, pulse amplitude of 25 mV, scan increment of 5 mV for SWV measurements) (n = 6)

$$\text{Limit of detection} = 3.3S/m \quad (2)$$

Herein, S stands for the intercept's standard deviation, while m is the slope of the regression line. In terms of sensitivity and linearity, Table 1 shows how the constructed electrochemical AFP immunosensor surpassed existing techniques. Initially, in comparison to any of the other approaches, the sensitive electrochemical AFP detection with a LOD of 3.30 fg mL^{-1} was accomplished satisfactorily. Moreover, the proposed synthetic strategy of MNPs@SiO_2@TiO_2, and Fe_3O_4NPs@COF/AuNPs in immunosensor construction was especially time-efficient and environmentally benign. As a consequence, it can be speculated that considering its outstanding electroanalytical performance, the fabricated immunosensor was of substantial potential for AFP detection.

Recovery

Four separate plasma samples (plasma sample1, plasma sample2, plasma sample3, and plasma sample4) were prepared for the recovery studies. The characteristics of solutions are represented in the Supplementary Data file. The close to 100.00% values in Table S1 of recovery studies verified the electrochemical immunosensor's exceptional accuracy, allowing for successful AFP detection without interference. To validate the excellent selectivity for plasma samples, the standard addition procedure was also conducted, and the calibration equation was derived as follows: I (µA) = 22.917C_{AFP} (pg mL^{-1}) + 10.084 R^2 = 0.9998. Thereby, both the close slope values between direct

Table 1 The collation of the electrochemical performance metrics of the fabricated immunosensor with other contemporary procedures

Material/Method	Linear range	LOD	Ref
MIL-101(Cr)/CdSeQDs	0.10–300.0 ng mL^{-1}	0.054 ng mL^{-1}	[3]
Eu-MOF@AuNPs	0.002–15.0 ng mL^{-1}	0.16 pg mL^{-1}	[22]
SERS	1.00 pg mL^{-1}–10.0 ng mL^{-1}	0.03 pg mL^{-1}	[60]
AuNS@Ag@SiO_2	3.00 pg mL^{-1}–3.00 μg mL^{-1}	0.72 pg mL^{-1}	[61]
Fe_3O_4@AuNPs	1.00–200.0 ng mL^{-1}	0.65 ng mL^{-1}	[62]
Thionine-AuNPs	0.05–100.0 ng mL^{-1}	0.012 ng mL^{-1}	[63]
CdTeQDs/TiO_2	0.50 pg mL^{-1}–10.00 μg mL^{-1}	0.13 pg mL^{-1}	[64]
N-GQDs	0.005–100.0 ng mL^{-1}	1.20 pg mL^{-1}	[65]
PdAg NDs/CoFe PBA	100.00 fg mL^{-1}–200.00 ng mL^{-1}	18.60 fg mL^{-1}	[23]
Sandwich-type immunosensor	***0.01–1.00 pg mL^{-1}***	***3.30 fg mL^{-1}***	***This study***

MIL-101(Cr)/CdSeQDs, metal organic frameworks/cadmium selenide quantum dots; *Eu-MOF@AuNPs*, gold nanoparticle–modified europium-metal organic frameworks; *SERS*, surface-enhanced Raman spectroscopy; *AuNS@Ag@SiO_2*, silica-coated gold/silver core–shell nanostars; *Fe_3O_4@AuNPs*, iron oxide@gold nanoparticles; *Thionine-AuNPs*, thionine-gold nanoparticles; *CdTeQDs/TiO_2*, CdTe quantum dots/titanium dioxide; *N-GQDs*, nitrogen-doped graphene quantum dots; *PdAg NDs/CoFe PBA*, PdAg nanodendrites modified CoFe Prussian blue analog.

calibration (inset of Fig. 5) and standard addition approach confirmed the selective AFP assay.

The validity of the electrochemical AFP immunosensor was evaluated by SERS [60] and when the comparison results (Table S2) were investigated, there was no important difference between the two methods ($T_{calculated} > T_{tabulated}$, $p > 0.05$).

Performance evaluation of the fabricated immunosensor

The performance of the fabricated AFP immunosensor was investigated in terms of its selectivity, stability, repeatability, and reusability values. In this regard, ten distinct electrochemical AFP immunosensors were constructed to illustrate the enhanced selectivity of electrochemical immunosensors. The prepared protein solutions were used to test the electrochemical AFP immunosensors. With this purpose, the following solutions were utilized: (i) 200.00 pg mL^{-1} PSA + 200.00 pg mL^{-1} BSA + 200.00 pg mL^{-1} CEA, (ii) 0.500 pg mL^{-1} AFP + 200.00 pg mL^{-1} PSA, (iii) 0.500 pg mL^{-1} AFP + 200.00 pg mL^{-1} BSA, (iv) 0.500 pg mL^{-1} AFP + 200.00 pg mL^{-1} CEA, (v) 0.500 pg mL^{-1} AFP + 200.00 pg mL^{-1} SCCA, (vi) 0.500 pg mL^{-1} AFP + 200.00 pg mL^{-1} HSA, (vii) 0.500 pg mL^{-1} AFP + 200.00 pg mL^{-1} NSE, (viii) 0.500 pg mL^{-1} AFP + 200.00 pg mL^{-1} IgG, (ix) 0.500 pg mL^{-1} AFP + 200.00 pg mL^{-1} L-CYS, and (x) 0.500 pg mL^{-1} AFP + 200.00 pg mL^{-1} GLU in the presence of 1.0 mM H_2O_2 solution. Figure S5A verifies that the other proteins (PSA, BSA, CEA, SCCA, HSA, NSE, IgG, L-CYS, and GLU) had no effect on the performance of the highly selective electrochemical AFP detection [66].

The collection of SWV data (Fig. S5B) over a 7-week period further revealed the electrochemical immunosensor's remarkable stability. As per Fig. S5B, the acquired current signal at the end of the seventh week was about 99.18% of the signal collected at the end of the 1st week, showing the excellent stability of the constructed electrochemical AFP immunosensor.

To assess the repeatability of the immunosensor, 30 individual electrochemical AFP immunosensors were constructed according to the previously described approach in the immunosensor fabrication sections. The relative standard deviation of the recorded current signals was determined to be 0.19%, implying the satisfactory reliability of the protocol of immunosensor fabrication.

Finally, the reusability feature of the fabricated AFP immunosensor was assessed. Over the 30 times utilization of the fabricated immunosensor, the relative standard deviation (RSD) value of the recorded current signals was computed to be 0.19%, proving a significant reusability level.

Conclusions

In this work, a reliable, selective, and sensitive electrochemical AFP immunosensor was constructed based on GCE modified Fe_3O_4NPs@COF/AuNPs to immobilize a particular anti-AFP capture antibody for antigen AFP recognition, and MNPs@SiO_2@TiO_2 for signal amplification. The fabricated immunosensor demonstrated the simple use of the immunosensor in the early detection of cancer. In addition, the proposed electrochemical AFP immunosensor showed superior stability, repeatability, and reusability features, providing long-term availability. Moreover, the developed immunosensor has a highly selective ability in

electrochemical AFP detection in the presence of other proteins. This study may pave the way for the engineering and design of a highly selective and sensitive electrochemical immunosensor for cancer detection in its early stages.

Supplementary Information The online version contains supplementary material available at https://doi.org/10.1007/s00604-022-05344-z.

Declarations

Conflict of interest The authors declare no competing interests.

References

1. Srinivas PR, Kramer BS, Srivastava S (2001) Trends in biomarker research for cancer detection. Lancet Oncol 2(11):698–704
2. Giannetto M, Elviri L, Careri M, Mangia A, Mori G (2011) A voltammetric immunosensor based on nanobiocomposite materials for the determination of alpha-fetoprotein in serum. Biosens Bioelectron 26(5):2232–2236
3. Zhong XL, Zhang M, Guo LA, Xie YZ, Luo RF, Chen WX, Cheng FL, Wang LS (2021) A dual-signal self-checking photoelectrochemical immunosensor based on the sole composite of MIL-101(Cr) and CdSe quantum dots for the detection of alpha-fetoprotein. Biosens Bioelectron 189:113389
4. Li N, Ma HM, Cao W, Wu D, Yan T, Du B, Wei Q (2015) Highly sensitive electrochemical immunosensor for the detection of alpha fetoprotein based on PdNi nanoparticles and N-doped graphene nanoribbons. Biosens Bioelectron 74:786–791
5. Teramura Y, Iwata H (2007) Label-free immunosensing for alpha-fetoprotein in human plasma using surface plasmon resonance. Anal Biochem 365(2):201–207
6. Zhou F, Li ZY, Bao ZT, Feng K, Zhang Y, Wang T (2015) Highly sensitive, label-free and real-time detection of alpha-fetoprotein using a silicon nanowire biosensor. Scand J Clin Lab Inv 75(7):578–584
7. Bader D, Riskin A, Vafsi O, Tamir A, Peskin B, Israel N, Merksamer R, Dar H, David M (2004) Alpha-fetoprotein in the early neonatal period - a large study and review of the literature. Clin Chim Acta 349(1–2):15–23
8. Wang XW, Xu B (1998) Stimulation of tumor-cell growth by alpha-fetoprotein. Int J Cancer 75(4):596–599
9. Lin JH, He CY, Zhang LJ, Zhang SS (2009) Sensitive amperometric immunosensor for alpha-fetoprotein based on carbon nanotube/gold nanoparticle doped chitosan film. Anal Biochem 384(1):130–135
10. Qu ZY, Xu H, Xu P, Chen KM, Mu R, Fu JP, Gu HC (2014) Ultrasensitive ELISA using enzyme-loaded nanospherical brushes as labels. Anal Chem 86(19):9367–9371
11. Qian J, Zhou ZX, Cao XD, Liu SQ (2010) Electrochemiluminescence immunosensor for ultrasensitive detection of biomarker using Ru(bpy)(3)(2+)-encapsulated silica nanosphere labels. Anal Chim Acta 665(1):32–38
12. Scarano S, Scuffi C, Mascini M, Minunni M (2010) Surface plasmon resonance imaging (SPRi)-based sensing: a new approach in signal sampling and management. Biosens Bioelectron 26(4):1380–1385
13. Shafik HM, Ayoub SM, Ebeid NH, Someda HH (2014) New adjuvant design using layered double hydroxide for production of polyclonal antibodies in radioimmunoassay techniques. J Radioanal Nucl Ch 301(1):81–89
14. Zhou L, Ji FH, Zhang T, Wang F, Li YC, Yu ZX, Jin XP, Ruan B (2019) An fluorescent aptasensor for sensitive detection of tumor marker based on the FRET of a sandwich structured QDs-AFP-AuNPs. Talanta 197:444–450
15. Wang GL, Yuan JL, Gong BL, Matsumoto K, Hu ZD (2001) Immunoassay by graphite furnace atomic absorption spectrometry using a metal chelate as a label. Anal Chim Acta 448(1–2):165–172
16. Darain F, Park SU, Shim YB (2003) Disposable amperometric immunosensor system for rabbit IgG using a conducting polymer modified screen-printed electrode. Biosens Bioelectron 18(5–6):773–780
17. Wang JN, Zhang SP, Dai H, Zheng HL, Hong ZS, Lin YY (2019) Dual-readout immunosensor constructed based on brilliant photoelectrochemical and photothermal effect of polymer dots for sensitive detection of sialic acid. Biosens Bioelectron 142:111567
18. Xie YZ, Zhang M, Bin QY, Xie SL, Guo LA, Cheng FL, Lv WZ (2020) Photoelectrochemical immunosensor based on CdSe@BiVO4 Co-sensitized TiO2 for carcinoembryonic antigen. Biosens Bioelectron 150:111949
19. Karaman O, Ozcan N, Karaman C, Yola BB, Atar N, Yola ML (2022) Electrochemical cardiac troponin I immunosensor based on nitrogen and boron-doped graphene quantum dots electrode platform and Ce-doped SnO2/SnS2 signal amplification. Mater Today Chem 23:100666
20. Karaman C, Yola BB, Karaman O, Atar N, Polat I, Yola ML (2021) Sensitive sandwich-type electrochemical SARS-CoV-2 nucleocapsid protein immunosensor. Microchim Acta 188(12):1–13
21. Chen Y, Yuan PX, Wang AJ, Luo XL, Xue YD, Zhang L, Feng JJ (2019) A novel electrochemical immunosensor for highly sensitive detection of prostate-specific antigen using 3D open-structured PtCu nanoframes for signal amplification. Biosens Bioelectron 126:187–192
22. Li H, Wang X, Zhang X, He M, Zhang J, Liu P, Tang X, Li C, Wang Y (2022) Eu-MOF nanorods functionalized with large heterocyclic ionic liquid for photoelectrochemical immunoassay of α-fetoprotein. Anal Chim Acta 7:339459
23. Tan M, Zhang C, Li Y, Xu Z, Wang S, Liu Q, Li Y (2022) An efficient electrochemical immunosensor for alpha-fetoprotein detection based on the CoFe Prussian blue analog combined PdAg hybrid nanodendrites. Bioelectrochemistry 145:108080
24. Zhu LP, Ye J, Yan MX, Yu LY, Peng Y, Huang JS, Yang XR (2021) Sensitive and programmable "signal-off" electrochemiluminescence sensing platform based on cascade amplification and multiple quenching mechanisms. Anal Chem 93(4):2644–2651
25. Kang X, Li YW, Zhu MZ, Jin RC (2020) Atomically precise alloy nanoclusters: syntheses, structures, and properties. Chem Soc Rev 49(17):6443–6514
26. Madhusudan P, Shi R, Xiang SL, Jin MT, Chandrashekar BN, Wang JW, Wang WJ, Peng OW, Amini A, Cheng C (2021) Construction of highly efficient Z-scheme ZnxCd1-xS/Au@g-C3N4 ternary heterojunction composite for visible-light-driven photocatalytic reduction of CO2 to solar fuel. Appl Catal B-Environ 282:119600
27. Holm A, Goodman ED, Stenlid JH, Aitbekova A, Zelaya R, Diroll BT, Johnston-Peck AC, Kao KC, Frank CW, Pettersson LGM, Cargnello M (2020) Nanoscale spatial distribution of supported nanoparticles controls activity and stability in powder catalysts for CO oxidation and photocatalytic H-2 evolution. J Am Chem Soc 142(34):14481–14494
28. Zhu L, Liang GL, Guo CP, Xu MR, Wang MH, Wang CB, Zhang ZH, Du M (2022) A new strategy for the development of efficient impedimetric tobramycin aptasensors with metallo-covalent organic frameworks (MCOFs). Food Chem 366:130575

29. Zhang ZH, Lou YF, Guo CP, Jia QJ, Song YP, Tian JY, Zhang S, Wang MH, He LH, Du M (2021) Metal-organic frameworks (MOFs) based chemosensors/biosensors for analysis of food contaminants. Trends Food Sci Tech 118:569–588
30. He HM, Zhu QQ, Yan Y, Zhang HW, Han ZY, Sun HM, Chen J, Li CP, Zhang ZH, Du M (2022) Metal-organic framework supported Au nanoparticles with organosilicone coating for high-efficiency electrocatalytic N2 reduction to NH3. Appl Catal B-Environ 302:120840
31. Gomez-Pastora J, Dominguez S, Bringas E, Rivero MJ, Ortiz I, Dionysiou DD (2017) Review and perspectives on the use of magnetic nanophotocatalysts (MNPCs) in water treatment. Chem Eng J 310:407–427
32. Mohammed L, Gomaa HG, Ragab D, Zhu J (2017) Magnetic nanoparticles for environmental and biomedical applications: a review. Particuology 30:1–14
33. Stanicki D, Elst LV, Muller RN, Laurent S (2015) Synthesis and processing of magnetic nanoparticles. Curr Opin Chem Eng 8:7–14
34. Laurent S, Forge D, Port M, Roch A, Robic C, Elst LV, Muller RN (2008) Magnetic iron oxide nanoparticles: synthesis, stabilization, vectorization, physicochemical characterizations, and biological applications. Chem Rev 108(6):2064–2110
35. Jeelani PG, Mulay P, Venkat R, Ramalingam C (2020) Multifaceted application of silica nanoparticles. A review Silicon-Neth 12(6):1337–1354
36. Stöber W, Fink A, Bohn E (1968) Controlled growth of monodisperse silica spheres in the micron size range. J Colloid Interface Sci 26(1):62–69
37. Byrne C, Subramanian G, Pillai SC (2018) Recent advances in photocatalysis for environmental applications. J Environ Chem Eng 6(3):3531–3555
38. Alvarez PM, Jaramillo J, Lopez-Pinero F, Plucinski PK (2010) Preparation and characterization of magnetic TiO2 nanoparticles and their utilization for the degradation of emerging pollutants in water. Appl Catal B-Environ 100(1–2):338–345
39. Katta KV, Dubey RS (2021) Comparative study of doped-TiO2 nanocrystals prepared by sol-gel and solvothermal approaches. Mater Today-Proc 39:1422–1425
40. Jahani PM, Beitollahi H, Tajik S, Tashakkorian H (2020) Selective electrochemical determination of bisphenol A via a Fe3O4 NPs derivative-modified graphite screen-printed electrode. Int J Environ an Ch 100(11):1209–1225
41. Xu YL, Shi XF, Hua R, Zhang R, Yao YJ, Zhao B, Liu T, Zheng JZ, Lu G (2020) Remarkably catalytic activity in reduction of 4-nitrophenol and methylene blue by Fe3O4@COF supported noble metal nanoparticles. Appl Catal B-Environ 260:118142
42. Yola ML, Atar N, Qureshi MS, Ustundag Z, Solak AO (2012) Electrochemically grafted etodolac film on glassy carbon for Pb(II) determination. Sensor Actuat B-Chem 171:1207–1215
43. Zhang L, Wu Z, Chen LW, Zhang LJ, Li XL, Xu HF, Wang HY, Zhu G (2016) Preparation of magnetic Fe3O4/TiO2/Ag composite microspheres with enhanced photocatalytic activity. Solid State Sci 52:42–48
44. Wang J, Yang JH, Li XY, Wei B, Wang DD, Song H, Zhai HJ, Li XF (2015) Synthesis of Fe3O4@SiO2@ZnO-Ag core-shell microspheres for the repeated photocatalytic degradation of rhodamine B under UV irradiation. J Mol Catal a-Chem 406:97–105
45. Yola ML, Atar N (2021) Novel voltammetric tumor necrosis factor-alpha (TNF-alpha) immunosensor based on gold nanoparticles involved in thiol-functionalized multi-walled carbon nanotubes and bimetallic Ni/Cu-MOFs. Anal Bioanal Chem 413(9):2481–2492
46. Medetalibeyoglu H, Beytur M, Akyildirim O, Atar N, Yola ML (2020) Validated electrochemical immunosensor for ultra -sensitive procalcitonin detection: Carbon electrode modified with gold nanoparticles functionalized sulfur doped MXene as sensor platform and carboxylated graphitic carbon nitride as signal amplification. Sensor Actuat B-Chem 319:128195
47. Yola ML, Atar N (2019) Development of cardiac troponin-I biosensor based on boron nitride quantum dots including molecularly imprinted polymer. Biosens Bioelectron 126:418–424
48. Li H, Kou BB, Yuan YL, Chai YQ, Yuan R (2022) Porous Fe3O4@COF-Immobilized gold nanoparticles with excellent catalytic performance for sensitive electrochemical detection of ATP. Biosens Bioelectron 197:113758
49. Xu H, Gao J, Jiang DL (2015) Stable, crystalline, porous, covalent organic frameworks as a platform for chiral organocatalysts. Nat Chem 7(11):905–912
50. Saeed M, Iqbal MZ, Ren WZ, Xia YZ, Liu C, Khan WS, Wu AG (2018) Controllable synthesis of Fe3O4 nanoflowers: enhanced imaging guided cancer therapy and comparison of photothermal efficiency with black-TiO2. J Mater Chem B 6(22):3800–3810
51. Hui C, Shen CM, Tian JF, Bao LH, Ding H, Li C, Tian YA, Shi XZ, Gao HJ (2011) Core-shell Fe3O4@SiO2 nanoparticles synthesized with well-dispersed hydrophilic Fe3O4 seeds. Nanoscale 3(2):701–705
52. Deng Y, Qi D, Deng C, Zhang X, Zhao D (2008) Superparamagnetic high-magnetization microspheres with an Fe3O4@SiO2 core and perpendicularly aligned mesoporous SiO2 shell for removal of microcystins. J Am Chem Soc 130(1):28–29
53. Fernandes IL, Barbosa DP, de Oliveira SB, da Silva VA, Sousa MH, Montero-Munoz M, Coaquira JAH (2022) Synthesis and characterization of the MNP@SiO2@TiO2 nanocomposite showing strong photocatalytic activity against methylene blue dye. Appl Surf Sci 580:152195
54. Jardim KV, Palomec-Garfias AF, Andrade BYG, Chaker JA, Bao SN, Marquez-Beltran C, Moya SE, Parize AL, Sousa MH (2018) Novel magneto-responsive nanoplatforms based on MnFe2O4 nanoparticles layer-by-layer functionalized with chitosan and sodium alginate for magnetic controlled release of curcumin. Mat Sci Eng C-Mater 92:184–195
55. Arman A, Saglam S, Uzer A, Apak R (2022) Electrochemical determination of nitroaromatic explosives using glassy carbon/multi walled carbon nanotube/polyethyleneimine electrode coated with gold nanoparticles. Talanta 238:122990
56. Kulpa A, Ryl J, Schroeder G, Koterwa A, Anand JS, Ossowski T, Niedzialkowski P (2020) Simultaneous voltammetric determination of Cd2+, Pb2+, and Cu2+ ions captured by Fe3O4@SiO2 core-shell nanostructures of various outer amino chain length. J Mol Liq 314:113677
57. Huang XB, Wang G, Yang M, Guo WC, Gao HY (2011) Synthesis of polyaniline-modified Fe3O4/SiO2/TiO2 composite microspheres and their photocatalytic application. Mater Lett 65(19–20):2887–2890
58. Yuan Q, Li N, Geng WC, Chi Y, Li XT (2012) Preparation of magnetically recoverable Fe3O4@SiO2@meso-TiO2 nanocomposites with enhanced photocatalytic ability. Mater Res Bull 47(9):2396–2402
59. Karaman C, Karaman O, Yola BB, Ulker I, Atar N, Yola ML (2021) A novel electrochemical aflatoxin B1 immunosensor based on gold nanoparticle-decorated porous graphene nanoribbon and Ag nanocube-incorporated MoS2 nanosheets. New J Chem 45(25):11222–11233
60. Er E, Sanchez-Iglesias A, Silvestri A, Arnaiz B, Liz-Marzan LM, Prato M, Criado A (2021) Metal nanoparticles/MoS2 surface-enhanced Raman scattering-based sandwich immunoassay for a-fetoprotein detection. Acs Appl Mater Inter 13(7):8823–8831
61. Zhao J, Wu C, Zhai LP, Shi XF, Li X, Weng GJ, Zhu J, Li JJ, Zhao JW (2019) A SERS-based immunoassay for the detection of alpha-fetoprotein using AuNS@Ag@SiO2 core-shell nanostars. J Mater Chem C 7(27):8432–8441

62. Liang RP, Yao GH, Fan LX, Qiu JD (2012) Magnetic Fe3O4@Au composite-enhanced surface plasmon resonance for ultrasensitive detection of magnetic nanoparticle-enriched alpha-fetoprotein. Anal Chim Acta 737:22–28
63. Alizadeh N, Salimi A, Hallaj R (2018) Magnetoimmunosensor for simultaneous electrochemical detection of carcinoembryonic antigen and α-fetoprotein using multifunctionalized Au nanotags. J Electroanal Chem 811:8–15
64. Li YJ, Ma MJ, Zhu JJ (2012) Dual-signal amplification strategy for ultrasensitive photoelectrochemical immunosensing of alpha-fetoprotein. Anal Chem 84(23):10492–10499
65. Zhang LN, Li L, Ma C, Ge SG, Yan M, Bian CR (2015) Detection of alpha-fetoprotein with an ultrasensitive electrochemiluminescence paper device based on green-luminescent nitrogen-doped graphene quantum dots. Sensor Actuat B-Chem 221:799–806
66. Li H, Wang X, Zhang X, He M, Zhang J, Liu P, Tang X, Li C, Wang Y (2022) Eu-MOF nanorods functionalized with large heterocyclic ionic liquid for photoelectrochemical immunoassay of alpha-fetoprotein. Anal Chim Acta 1195:339459